Higher Power Density Decoupled Magnetic Device With Core Integrated Orthogonal Windings for Power Converters

Shamroze Fayyaz, Umair Munir, Mohamed Atef Tawfik, Kyoung-Tak Kim, Jong-Kwon Jeon, Ashraf Ahmed, *Member, IEEE*, and Joung-Hu Park, *Senior Member, IEEE*

***Abstract*—This article proposes a three-plate, leg-less magnetic structure for integrated magnetic device to enhance the power density of the power electronics converters. The main idea could be used to integrate any magnetic device, such as decoupled inductors, decoupled transformers, or decoupled inductor with transformer, in the same core. In this article, a case of two decoupled inductors integrated in the same core using two orthogonal windings is presented. The proposed magnetic device features two inductive coils, wound on a single magnetic core, arranged perpendicularly in three-dimensional space. This specific configuration ensures nearly zero magnetic coupling between the coils, effectively transforming the integrated magnetic device into two independent inductors with higher power density. The three-plate structure distributes the magnetic flux in a more uniform manner, mitigating magnetic concentration within the structure. The uniform distribution of magnetic flux enables the device to handle stronger H-fields before reaching saturation, thus increasing the power density of the device. The design holds promise for various dc–dc converter applications, potentially leading to cost and size reduction with higher power density. The article provides a comprehensive analysis of the magnetic performance of the proposed magnetic device through detailed finite element method simulations. The magnetic performance of the proposed device is compared with that of the recently proposed two-plate, quadratic-legs structure. The adoption of the three-plate design led to a 25% reduction in the magnetic flux density, for the same load conditions, enabling the device to handle 60% higher current than the quadratic-legs structure. A prototype, tested using a 250 W 2-phase interleaved boost converter and compared with discrete core inductors, revealed that the proposed device achieved a 50% reduction in the volume of the magnetic component of the system without compromising system efficiency, which remained consistent at 94% for both discrete core inductors and the proposed magnetic device.**

***Index Terms*—Core integration, dc–dc converters, high power density, integrated inductor, interleaved converters, magnetic device, orthogonal windings.**

Received 30 July 2024; revised 31 October 2024; accepted 30 November 2024. Date of publication 4 December 2024; date of current version 28 January 2025. This work was supported by the National Research Foundation of Korea, under Grant 2019R1A2C1084605. Recommended for publication by Associate Editor J. Alonso. *(Corresponding author: Joung-Hu Park.)*

The authors are with the Department of Electrical Engineering, Soongsil University, Seoul 06978, Korea (e-mail: shamroze.f@gmail.com; umairmunir3@gmail.com; m.atef210@yahoo.com; chiiwhite@gmail.com; dtf986@naver.com; ahmed@ssu.ac.kr; wait4u@ssu.ac.kr).

Color versions of one or more figures in this article are available at https://doi.org/10.1109/TPEL.2024.3510719.

Digital Object Identifier 10.1109/TPEL.2024.3510719

I. Introduction

THE power electronics industry is consistently striving for increased efficiency, cost reduction, and more compact designs. Significant investments are dedicated to the development of advanced, cost-effective devices, efficient topologies, and effective control strategies [1]. Meeting the diverse power requirements and applications of the modern power electronics sector involves a continuous emergence of various converter and inverter types [2]. Additionally, the utilization of the industrial, scientific, and medical band frequencies has enabled the realization of smaller, more compact devices suitable for integration [3].

DC–DC converters are extensively used in industry, serving a wide range of applications from integrating renewable energy sources, to powering electric vehicle systems and medical devices, in addition to being employed in various military applications [4]. To meet high power demands, interleaving multiple converters is a common practice, enhancing efficiency while reducing device current ratings and the ripple [5].

A simple example of an interleaved dc–dc converter is the two-phase interleaved boost converter, as shown in Fig. 1(a). Conventional dc–dc converters face challenges such as high voltage and current stresses across switches and substantial current flow through the inductor [6]. Interleaved dc–dc converters address these issues by incorporating additional inductors and switches. However, it is essential to note that interleaving dc–dc converters with additional inductors, such as discrete core inductors, as shown in Fig. 1(b), results in a significant increase in volume, weight, and overall cost compared to the conventional single-phase topology. Moreover, as the demand for base metals and rare earth metal rises due to the global economic growth [7], there is a pressing need to reduce the size of magnetic components in interleaved converters for cost-effectiveness and sustainability in industry.

Therefore, recent research has focused on improving the performance of magnetic devices in power electronics' topologies to achieve higher power density, enhanced compactness, and lower magnetic losses. The use of nanocrystalline cores instead of ferrite cores has emerged in recent years due to their advantage of higher magnetic permeability and lighter weight [8], [9]. Replacing solid or litz wires for winding inductive coils with carbon nanotubes (CNT) based conductors at high frequencies

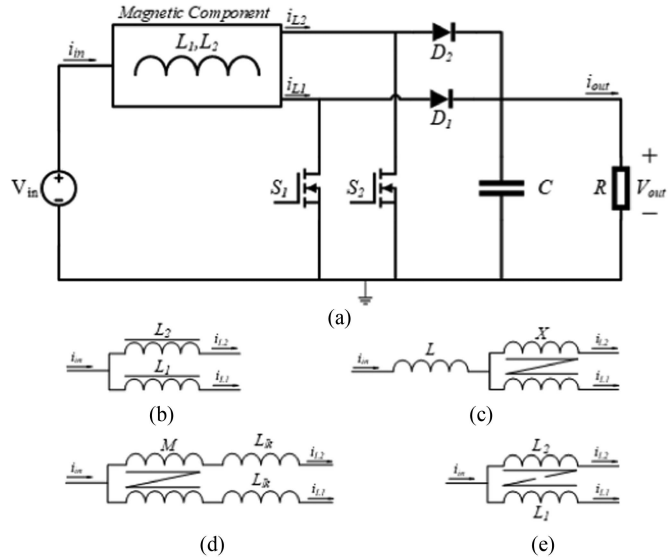

Fig. 1. Generic interleaved boost converter topology with various magnetic component strategies. (a) Two-phase interleaved boost converter circuit. (b) Discrete core inductors. (c) Coupled inductors. (d) Integrated magnetics coupled inductors. (e) Integrated magnetics decoupled inductors.

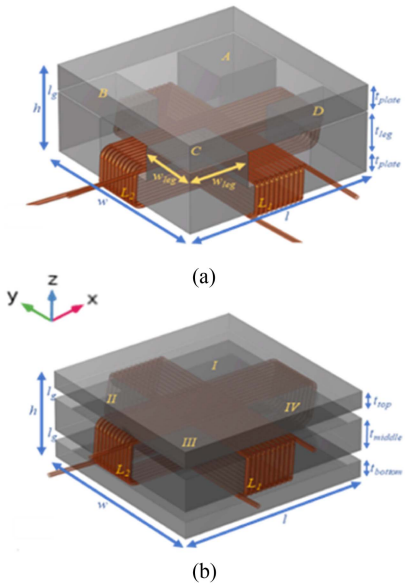

Fig. 2. Three-dimensional view of; (a) two-plate, quadratic-legs magnetic structure with orthogonal windings, (b) the proposed three-plate leg-less magnetic structure as integrated inductive device with orthogonal windings.

has also been studied in [10], [11], and [12] and shown that CNT-based conductors can perform better at high frequencies in terms of resistance. However, conventional copper coils and ferrite cores still dominate the industrial sector, as well as remain the main focus of research.

The performance of coupled inductors (see Fig. 1(c) XL) has been investigated and shown to be more favorable than decoupled inductors [13], [14], [15]. Coupled inductors are often used with dc–dc converters, which allow the flexibility of controlling the voltage gain by controlling the turns ratio of the coupled integrated device [16]. However, despite reducing voltage stress on semiconductor devices, coupled inductors introduce some leakage inductance into the operation of the converter. Extensive studies on coupled inductors for interleaved converters, such as the 2001 research on integrated coupled inductors with a coupling coefficient as high as 0.98, demonstrated their ability to mitigate current imbalances between interleaved phases and enhance system performance [17]. However, achieving such a high level of coupling in practical applications remains a challenge. In cases of lower coupling, leakage inductance becomes more prominent, resulting in energy losses and high-voltage spikes during switching events. This necessitates the use of clamping circuits to manage voltage stress and, in some cases, recover the energy lost due to leakage inductance [18], [19], [20], [21], [22], [23], [24]. While coupled inductors are often regarded for their ability to reduce component count and minimize the overall size of converters, their dependency on clamping circuits introduces several trade-offs. These circuits not only negate the benefits of size and component reduction but also add complexity, cost, and footprint to the overall design. Furthermore, maintaining sufficient magnetizing inductance in coupled designs requires a higher number of turns, which increases interwinding capacitance and leads to greater energy losses [25].

Integrated magnetics is a magnetic component design methodology by which two or more magnetic components can be combined into a single magnetic core, reducing size, and cost. Integrated magnetics component can have coupling (see Fig. 1(d) IMXL) or no coupling (see Fig. 1(e) IM2L), present between the respective coils. Various design methodologies aim to enhance the performance of integrated magnetic devices, with air-gap optimization being one of them, reducing losses in integrated coupled inductors [26]. Integrating techniques using conventional E cores have been explored in [27]. Beyond the interleaving of the electrical circuit, the magnetic circuit is also interleaved to achieve comprehensive integration. Decoupling is accomplished by carefully controlling the flux flow within the core through precise distribution of the air gap across different core sections. It has been demonstrated that decoupled inductors with alternate coupling can significantly reduce device size by up to 45% and decrease core losses. An innovative twisted winding, inversely coupled inductor design has recently been presented in [28] for embedding in motherboards. This design is complex and its applicability across various fields is limited due to the unconventional core geometry required.

Conversely, the performance of decoupled integrated inductors in conjunction with dc–dc converters has not been thoroughly studied in the literature. Recently, a two-plate, quadratic-leg cubic magnetic core structure for decoupled inductors was proposed for an interleaved buck converter [29]. The decoupling between the inductive coils was achieved by arranging the coils perpendicularly in space around a single magnetic plate. Four legs were placed at each corner, connecting the bottom plate with the coils to a top plate. Fig. 2(a) illustrates the two-plate, quadratic-leg structure with the decoupled inductors. This structure is based on a concept from another study [30], which proposed decoupling primary windings in integrated

multiple-winding transformers using three-dimensional (3-D) space orthogonal flux. The study introduced the "four quadrants integrated transformers", which allows independent operation of input power stages, optimizing input source utilization, and simplifying system structure. In [31], a similar four leg structure is used to make a current balancing transformer for dc–dc converters by using inverse coupling to automatically achieve balancing between currents. Their approach to current balancing transformers in two-phase synchronous dc–dc converters presents principles that could be adapted to mitigate ripple effects, even in configurations involving decoupled inductors.

The two coils when arranged orthogonally can operate simultaneously with no magnetic coupling between them. The resultant magnetic flux density within the core structure is the vector sum of the respective perpendicular magnetic flux densities. However, the legs experience scalar summation of magnetic fluxes due to the similar axial direction. Consequently, the magnetic flux density within the legs can reach much higher intensity, causing losses to the performance of the device. The winding window for the inductive coils limits the thickness of the legs, which can be used to lower flux concentration within the legs.

Therefore, this article proposes an improved design of the cubic, planar magnetic structure consisting of a three-plate, legless magnetic core with two orthogonally wound inductive coils around the central plate, as shown in Fig. 2(b). The quadratic legs of the previous structure have been transformed into a third plate to ensure uniformity of the magnetic flux through the core, lower the magnetic flux density within the core structure, and enhance power density. A similar three-plate cubic magnetic structure is proposed in [32] for decoupled inductors. In that design, decoupling is achieved by winding the coils around the top and bottom plates, using the middle plate as a magnetic short. The presence of an air gap between the plates ensures that the magnetic fluxes of the respective inductors do not interact under normal operating conditions. However, coupling arises between the coils when the magnetic device reaches saturation, as the reluctance of the center plate becomes comparable to the reluctance of the air gap, leading to flux interaction. In contrast, the proposed design positions the windings orthogonally on the central plate, promoting better flux distribution and reducing the likelihood of flux crowding and saturation effects by distributing the flux among the three plates of the store more evenly, achieving decoupling between the orthogonal windings through spatial positioning of the coils. A three-plate magnetic structure using I-cores is proposed for Hybridge topology in [33]. However, the I-cores used have high permeability material on the edges of the plates which will attract magnetic flux lines causing flux crowding and potential saturation.

The rest of this article is organized as follows. In Section II, theoretical background is provided, including the decoupling effect, the dynamics of magnetic flux and the distribution of magnetic flux density across the core. The magnetic performance of the quadratic-legs structure and the proposed three-plates, leg-less structure is analyzed and compared using finite element method (FEM) simulations in Section III. The hardware prototype is tested using an interleaved boost converter and the results are presented in Section IV, along with a comparison of the proposed device to discrete inductors. Finally, Section V concludes this article.

II. Conceptual Framework

The interleaving of multiple phases of a dc–dc converter leads to a significant increase in volume and weight of the converter because of the additional inductors employing discrete magnetic cores, which finally reduces the power density of the magnetic device. Therefore, in this article, an integrated magnetics approach for the device is used to reduce the size of the interleaved converter, by making two inductors share the same magnetic core resulting in higher power density for the magnetic component and the converter.

A. Integrated Magnetic Device

The integrated magnetic device structure consists of three planar, stacked magnetic plates. The inductive coils are wound around the middle plate, orthogonal to each other. In order to strengthen the mechanical reliability of the structure, four legs, made of nonmagnetic material, are placed at the quadrants, between two adjacent plates. Fig. 2(b) illustrates the 3-D view of the three-plate structure. To eliminate potential confusion with the two-plate, quadratic-leg structure, the nonmagnetic legs are omitted as they do not play a role in the magnetic performance of the device. Henceforth, the proposed three-plate device is named as the "leg-less" device.

The following analysis is presented under the assumptions:

1) the two inductive coils have the same number of turns;
2) the two inductive coils have the same inductance;
3) the magnetic core is symmetrical;
4) 50% duty cycle;
5) boundary conduction mode or discontinuous conduction mode (DCM) operation only.

The decoupling effect arises from the fact that the magnetic flux from one coil flows perpendicularly to the cross-sectional area of the other coil due to the orthogonal arrangement of the two coils in space, as explained by Faraday's law of induction in (1) [34], which states that the induced EMF ε in a conductor is greatest when both the magnetic flux density vector, $\boldsymbol{B}$ and the area vector, $\boldsymbol{dA}$ are in the same direction ($\theta = 0°$) and zero if they are perpendicular to each other ($\theta = 90°$)

$$\varepsilon = -\frac{d\phi_B}{dt} = -\frac{d}{dt}\iint \boldsymbol{B}.\boldsymbol{dA} = -\frac{d}{dt}\iint B\cos\theta dA. \quad (1)$$

Fig. 3 visualizes a generalized behavior of magnetic field within the middle ferrite plate. The solid line arrows over the windings show the current flow direction through the windings. The center plate can be divided into four quadrants, separated by two perpendicular windings. The dashed arrows show the magnetic flux flow within the center plate. Considering instantaneous current flow and in-phase operation, as shown in Fig. 5(b), both the inductor current i_{L1} and i_{L2} reach their maximum at the same instant, t_0 in Fig. 5(b). Consequently, the magnetic flux density, B-field also reaches the peak magnitude at the same instant. Therefore, quadrants I and III experience perfect magnetic flux

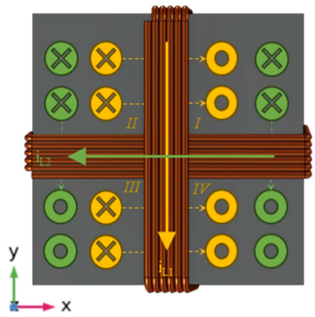

Fig. 3. Planar view of the middle plate. Arrows on the windings represent the current flow. The dashed arrows show the magnetic flux flow within the plate. Dot (.) and cross (x) notation indicate the flux direction in the z-axis. The roman numerals are for the quadrants.

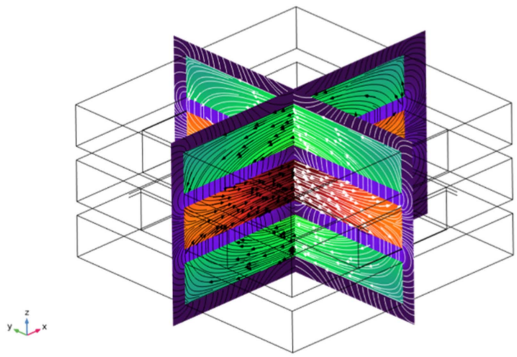

Fig. 4. Magnetic flux flow within the three-plate structure. The black arrows show the direction of the flux within the xz plane and white arrows lie in the yz plane.

cancellation, while summation of magnetic flux occurs within quadrants II and IV. As a result, the effective B-field flows diagonally through the magnetic core. If the currents are 180° out-of-phase, as shown in Fig. 5(a), at any given instant of time, one of the B-fields due to a single inductor increases while the other decreases. At the peak current value, t_0 for L_1 and t_1 for L_2 in Fig. 5, only a single inductor is responsible for the presence of B-field within the plates. Similar behavior regarding the flow of magnetic flux can be observed in the top and bottom plates, with the direction of the flux reversed compared to that in the middle plate.

The magnetic flux flows uniformly through the three plates of the magnetic core and is divided equally between the top and bottom plates as it flows out of the middle plate, as shown in Fig. 4. The middle plate's magnetic flux is the sum of the magnetic fluxes in the outer two plates. Therefore, the magnetic flux density in the middle plate is much higher than the other two plates. Thus, it is desirable to have a thicker middle plate than the outer two plates.

Considering the fringing effect, for a rectangular air gap with length, l, width, w and air gap length l_g, and absolute permeability μ_o (4π x 10^{-7} H/m), the ratio of the cross-sectional area of the fringing flux A_f to the cross-sectional area of the air gap, A_g, is given by (2). The ratios, $\alpha = w_f / l_g$ and $\beta = l_f / l_g$, are the mean width of the cross-sectional area of the fringing flux w_f and the mean path length of the fringing flux l_f to the air-gap length l_g, respectively. The fringing flux factor F_f for a rectangular air gap is given by (3). For the proposed leg-less structure, α and β range from 1–1.67 and 2–2.68, respectively. These constants were determined through experimental testing and practical evaluation. Consequently, the fringing flux factor F_f ranges from 1.3–1.5. The fringing flux factor increases the inductance of the device by reducing the reluctance by the fringing flux factor [35]. Therefore, the reluctance of the top plate or the bottom plate, $\Re_{g\text{top}}$ or $\Re_{g\text{bottom}}$, respectively, is given by (5) [36]. Equations (4) and (6) describe the spatially averaged magnetic flux within top plate $\Phi_{B\text{top}}(t)$, bottom plate $\Phi_{B\text{bottom}}(t)$, and middle plate $\Phi_{B\text{middle}}(t)$. N is the number of turns of the inductive coil and $i_L(t)$ is the inductor current. $\Re_g$ is the total air gap reluctance, given by (7), which is equal to a half of the top or bottom reluctance, $\Re_{g\text{top}}$ or $\Re_{g\text{bottom}}$, given by (5), due to parallel connection.

The design of the integrated magnetic device structure for a two-phase interleaved converter begins with calculating the input current, $I_{\text{in}} = P/V_{\text{in}}$, and dividing it equally across the phases to find $I_{\text{phase}} = I_{\text{in}}/2$. The peak current $I_{\text{pk}} = I_{\text{phase}} + \Delta I/2$ and ripple current ΔI are derived based on the inductance L, switching frequency f_{sw}, and input voltage V_{in}. Coil material selection, either round wire or foil, depends on the application, with foil windings allowing for smaller air gaps. Wire diameter (d_{wire}) or foil thickness (t_{foil}) is determined by the current per phase, and the minimum air gap length is calculated as $l_{g,\min} = 2d_{\text{wire}}$ (or $2t_{\text{foil}}$) $+ t_{\text{insulation}}$. The air gap area A_g is computed using energy equations, ensuring the maximum flux density B_{pk} stays below the core saturation limit. The plates' surface area, derived from A_g, and air gap reluctance, are used to calculate the number of turns $N = L/R_g$. The middle plate's cross-sectional area $A_{c,\text{middle}}$ and thickness are based on flux and saturation constraints, while the outer plates are sized at half the thickness of the middle plate

$$\frac{A_f}{A_g} = \frac{2\alpha l_g\,(l + w + 2\alpha l_g)}{lw} \tag{2}$$

$$F_f = 1 + \frac{A_f}{A_g}\,\frac{1}{\beta} = 1 + \frac{2\alpha l_g\,(l + w + 2\alpha l_g)}{\beta lw} \tag{3}$$

$$\Phi_{B_{\text{top}}}(t) = \Phi_{B_{\text{bottom}}}(t) = \frac{N i_L(t)}{\Re_{g_{\text{top,bottom}}}} \tag{4}$$

$$\Re_{g_{\text{top}}} = \Re_{g_{\text{bottom}}} = \frac{4 l_g}{\mu_o F_f A_g} \tag{5}$$

$$\Phi_{B_{\text{middle}}}(t) = \frac{N i_L(t)}{\Re_g} = \Phi_{B_{\text{top}}}(t) + \Phi_{B_{\text{bottom}}}(t) \tag{6}$$

$$\Re_g = \Re_{g_{\text{top}}} \parallel \Re_{g_{\text{bottom}}} = \frac{\Re_{g_{\text{top,bottom}}}}{2}. \tag{7}$$

B. Magnetic Flux Density

Magnetic flux density, B-field, represents the distribution of magnetic flux across the cross-sectional area of magnetic plates. Given that the generated magnetic flux is directly proportional to the inductor current flowing through the inductive coil, the B-field is inherently contingent on the inductor current. Moreover, the integrated structure encompasses two inductive coils, thereby introducing a dependence of the effective magnetic flux

TABLE I
EFFECTIVE MAGNETIC FLUX DENSITY

	B_{eff}	$B_{eff_{max}}$	$B_{eff_{min}}$	$f_{B_{eff}}$
In-Phase	$\sqrt{2}B_{L1,2}$	$\sqrt{2}B_{L1,2_{max}}$	$\sqrt{2}B_{L1,2_{min}}$	$f_{B_{L1,2}}$
Out-of-Phase	$\sqrt{{B_{L1}}^2 + {B_{L2}}^2}$	$B_{L1,2_{max}}$	$\sqrt{2}B_{avg}$	$2f_{B_{L1,2}}$

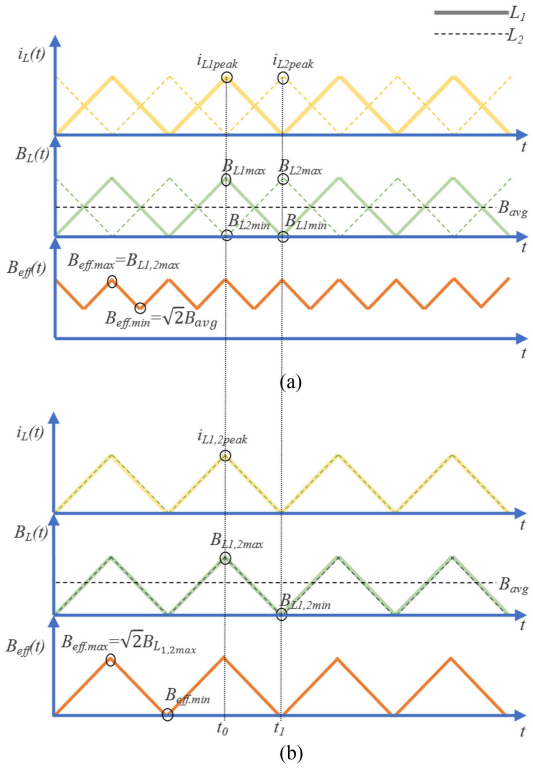

Fig. 5. Magnetic flux density with respect to the inductor current at 0.5 duty ratio, within the three-plate, leg-less structure. (a) 180° out-of-phase currents. (b) In-phase currents.

density within the magnetic structure on the phase difference between the two currents.

If $B_{L1}(t)$ denotes the magnetic flux density generated by coil L_1 and $B_{L2}(t)$ represents the magnetic flux density generated by coil L_2, each across the cross-sectional area, A_c of the plate, as the current, $i_L(t)$ passes through the coils, the effective magnetic flux density $B_{eff}(t)$, inside the magnetic core is the vector summation of the respective B-fields due to the orthogonal flow of magnetic flux and is given by (8) (see Table I). Equation (9) can be used to calculate the respective magnetic flux densities $B_{L1}(t)$ and $B_{L2}(t)$ [37]

$$B_{eff}(t) = \sqrt{(B_{L1}(t))^2 + (B_{L2}(t))^2} \tag{8}$$

$$B_{L1}(t) = B_{L2}(t) = \frac{L_{1,2} i_{L_{1,2}}(t)}{N A_c}. \tag{9}$$

If there is no phase difference between the two inductor currents, as in Fig. 5(b), both the generated magnetic flux densities by inductors 1 and 2, $B_{L1}(t)$ and $B_{L2}(t)$ would reach their maximum values, $B_{L1\max}$ and $B_{L2\max}$, at the maximum inductor current, $i_{L1\,\mathrm{peak}}$ and $i_{L2\mathrm{peak}}$, respectively. At any given time and point in the magnetic structure, the effective magnetic flux density $B_{eff}(t)$ would be 41.4% higher than the magnetic flux density generated by only one inductor $B_{L1}(t)$ or $B_{L2}(t)$. Consequently, the saturation current, I_{sat}, for each inductor would decrease by 29.3%. Moreover, both the inductors' currents, $i_{L1}(t)$ and $i_{L2}(t)$ and the effective magnetic flux density, $B_{eff}(t)$ would reach their minimum value of zero simultaneously. The frequency of the effective B-field f_{Beff} would be equal to the frequency of respective flux densities $f_{BL1,2}$.

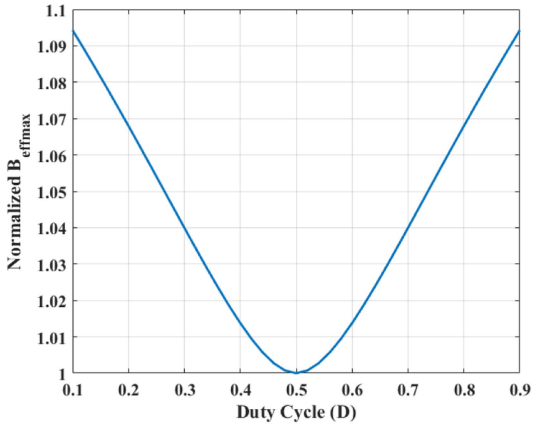

Fig. 6. Variation of normalized maximum effective magnetic flux density ($B_{\mathrm{eff,max}}$) with duty cycle (D), illustrating optimal performance at a 50% duty cycle and increased $B_{\mathrm{eff,max}}$ at duty cycles of 0.1 and 0.9.

If one of the inductor current is shifted 180° with respect to the other, the respective generated magnetic flux densities, $B_{L1}(t)$ and $B_{L2}(t)$ would also exhibit a 180° phase shift, as shown in Fig. 5(a). During the out-of-phase operation, the maximum effective magnetic flux density, $B_{eff\max}$ would be identical to $B_{L1\max}$ or $B_{L2\max}$, as only one inductor would contribute to the magnetic flux within the magnetic core structure at the maximum point. Due to the vector summation of the two magnetic flux densities, the effective B-field would never reach zero inside the core, and the minimum effective B-field would be half of the maximum B-field. Furthermore, the frequency of the effective B-field, f_{Beff} would be double that of the individual B-fields during out-of-phase operation (see Table I).

The graph provided (see Fig. 6) illustrates the relationship between the normalized maximum effective magnetic flux density ($B_{eff.\max}$) and the duty cycle (D). It demonstrates how $B_{eff.\max}$ varies across different duty cycles, highlighting the optimal performance at a 50% duty cycle.

From the graph (see Fig. 6), it is evident that $B_{eff.\max}$ is at its minimum at a 50% duty cycle. At this point, the effective magnetic flux density is normalized to a value of 1, indicating that the contribution from the interleaved inductors is perfectly balanced, thus achieving optimal performance.

At duty cycles other than 50%, $B_{eff.\max}$ increases on both sides. For example, at duty cycles of 0.1 and 0.9, the $B_{eff.\max}$ value is approximately 1.094, which is 9.4% greater than the value at 50%. This increase means that the effective magnetic

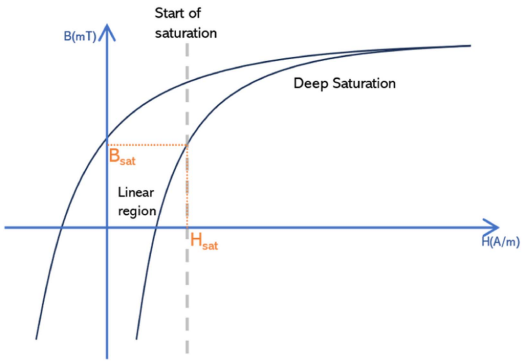

Fig. 7. Generic hysteresis (B-H) curve.

flux density exceeds the maximum value of a single inductor (B_L), leading to potential inefficiencies and increased magnetic stress on the components.

C. Saturation Point

Fig. 7 illustrates a general hysteresis loop with two sections separated by a dotted line. The left, linear part of the loop represents the desirable operating region for a magnetic core, corresponding to an increase in magnetic flux density, B with an increase in magnetic flux intensity H. As the magnetic flux intensity continues to rise, a point, H_{sat} is reached at the knee of the curve where further increase in H-field results in only a marginal increase in the B-field. This marks the onset of saturation for the core, as indicated by the dotted gray vertical line in Fig. 7. After this point, the magnetic permeability of the core reduces sharply, leading to a drop in inductance of the coil. Drop in inductance results in reduction of the impedance of the inductor, causing a sharp increase in the inductor current. The region to the right of the dotted line is the deep saturation region, characterized by the relatively flat part of the curve with very poor magnetic permeability and significantly higher magnetic reluctance.

Due to some multiple physical factors, such as uneven cross-sectional areas or windings windows, certain regions of the core may experience a concentration; high concentration of magnetic flux within a small area, leading to high magnetic flux density within that region. If the B-field of the hot spot region falls at the knee or further right in the curve, the region will exhibit lower magnetic permeability than the rest of the core and the higher magnetic reluctance. The higher reluctance will force the flux lines to drift apart to the surrounding regions with the lower magnetic reluctance. Hot spots might be limited to a small region of the core but depending on how extreme they are, the hot spots can increase the overall magnetic reluctance of the core and contribute to higher core losses.

The maximum inductor current that allows the inductor to operate within the linear region of the curve is denoted as I_{sat}. The saturation magnetic flux Φ_{Bsat} and the saturation magnetic flux density B_{sat} at I_{sat} can be calculated using (10) [37]. Depending on which plate's cross-sectional area is under consideration, Φ_{Bsat} can be $\Phi_{B\text{top}}$, $\Phi_{B\text{bottom}}$, or $\Phi_{B\text{middle}}$ and $\Re$ can be $\Re_{g\text{top}}$, $\Re_{g\text{bottom}}$, or $\Re_{\ g}$

$$B_{sat} = \frac{\Phi_{B_{sat}}}{A_c} = \frac{NI_{sat}}{\Re A_c}. \tag{10}$$

TABLE II
MAGNETIC DEVICE DIMENSIONS

Symbol	Quantity	Value
Quadratic-Legs Structure		
l	plate length	20 mm
w	plate width	20 mm
t_{plate}	plate thickness	3 mm
h	device height	10.4 mm
l_g	air gap length	0.4 mm
t_{legs}	legs' length	4 mm
w_{legs}	legs' width	6.5 mm
N	turns number	10
L_1, L_2	inductance	25.1 µH
Leg-Less Structure		
l	plate length	20 mm
w	plate width	20 mm
$t_{top,bottom}$	top/bottom plate thickness	2 mm
t_{middle}	middle plate thickness	4 mm
h	device height	10.4 mm
l_g	air gap length	1.2 mm
N	turns number	10
L_1, L_2	inductance	25.7 µH

III. NUMERICAL ANALYSIS

The performance of the proposed, three-plate, leg-less magnetic structure is compared with the two-plate, quadratic-legs structure. The magnetic flux behavior within the two structures is analyzed through COMSOL multiphysics. The core material remains consistent between the two integrated devices, maintaining an equivalent overall device volume. The two structures also have the same inductance for each coil, for the same number of turns. The dimensions for both the quadratic-leg and leg-less structures are mentioned in Table II.

A. Testing Environment

To verify the performance of the proposed leg-less magnetic device and compare it with a quadratic-leg magnetic device, FEM simulations were conducted using COMSOL multiphysics. The 3-D geometries of both inductor structures were created using COMSOL's geometry tool. The inductors were placed inside a cube-shaped air domain with an "infinite element domain condition" at the boundaries to mitigate reflection effects and more accurately replicate the physical hardware.

Predefined material properties were used for air and copper, while the properties of the ferrite core, specifically, material N97 from TDK, were manually inputted, including the permeability curve and hysteresis curve. The "magnetic fields (mf)" interface was utilized to compute parameters related to the magnetic fields around the coils, which were excited using the "electrical circuits (cir)" interface with current sources. Considering the worst-case condition for an orthogonally placed dual windings integrated decoupled inductor device, as explained earlier in Section II, in-phase currents were applied to the windings and the results were recorded at the peak current magnitude.

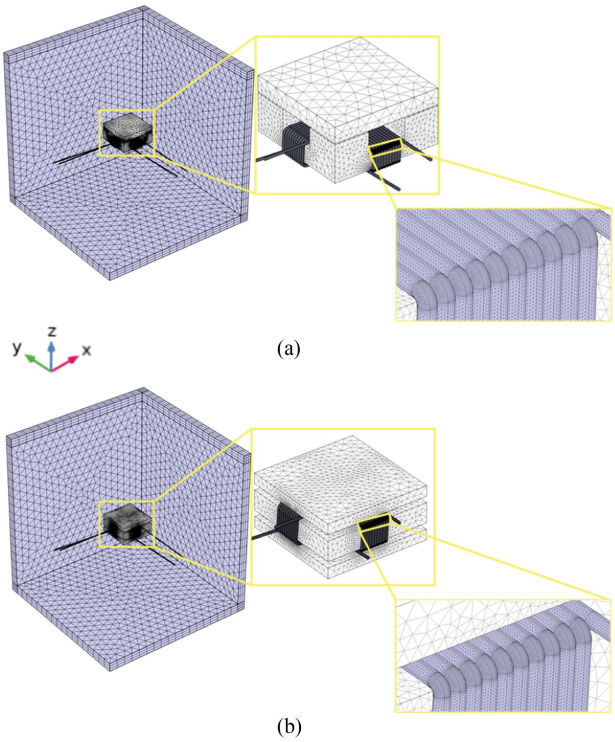

Fig. 8. Detailed COMSOL mesh visualization of the magnetic structures with variable mesh sizes tailored for different domains to enhance analysis accuracy. The front-facing three sides of the air domain are hidden for improved visibility of the internal mesh structure. (a) Quadratic-leg structure. (b) Leg-less structure.

The meshed geometries of both inductors are shown in Fig. 8. The model was solved in the frequency domain study using the iterative linear solver BiCGStab, with an error margin of 0.1%.

B. Magnetic Dynamics

Within the two magnetic structures, the magnetic flux flows diagonally through the magnetic plates due to the vector summation of the two equivalent orthogonal magnetic fluxes generated by the respective inductive coils. Within the magnetic plates, the effective magnetic flux density is also the vector sum of the orthogonal magnetic flux densities. However, within the legs of the quadratic-legs structure, the effective density is the scalar sum of the two individual magnetic fluxes because of the same axial direction. Due to scalar summation, two of the four legs have a higher concentration of magnetic flux than the rest of the structure, while the B-field is almost completely cancelled out in the other two legs, as shown in Fig. 9(a). The quadratic-legs structure exhibits extreme hot spots around the legs with flux summation. While the top and bottom plates for the quadratic-legs structure have relatively lower magnetic flux density, the high magnetic flux density within the legs can lead to higher overall losses. The spatially averaged magnetic flux density within the quadratic-leg structure is 0.16 T for excitation current of 5 A.

In contrast, the three-plate structure has significantly lower magnetic flux density due to an even air gap as evident in Fig. 9(b), for the same current through the inductive coils. The

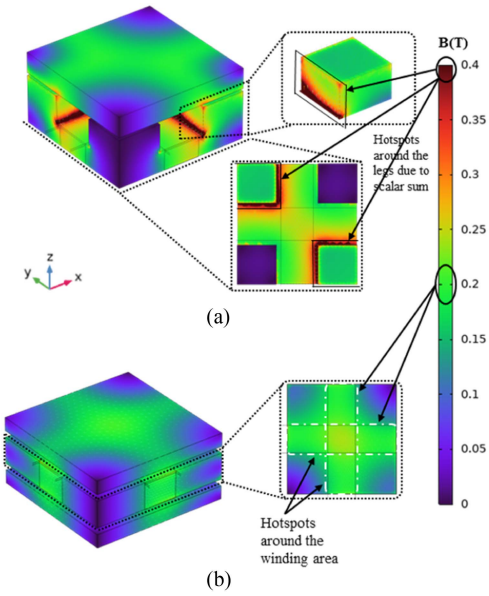

Fig. 9. Spatial B-field distribution for excitation current of 5 A_{peak}. (a) Quadratic-legs structure with extreme hotspots within two of the legs. (b) Leg-less structure with moderate hotspots around the winding area.

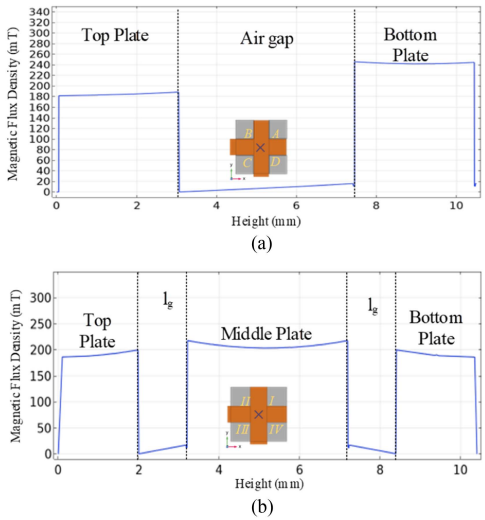

Fig. 10. Axial distribution of magnetic flux density along the z-axis, height of the structure for 5 A_{peak} current with "X" marking the point of measurement for center of; (a) quadratic-legs structure, (b) legless structure.

effective B-field in the entire volume of the magnetic structure is a vector summation of the perpendicular B-fields at any point and time. Some hot spots for the leg-less structure appear around the winding area. However, the intensity of magnetic flux density at these spots is significantly lower than the those of the quadratic-legs structure. The spatially average B-field of the entire leg-less structure is 0.12 T. The entire leg-less structure has 25% weaker average B-field than the entire quadratic-legs structure for the same excitation current.

Fig. 10 illustrates an axial B-field distribution with respect to the arc length (height) of the core structure for 5 A_{peak} of excitation current, with the arc length (height) through the center

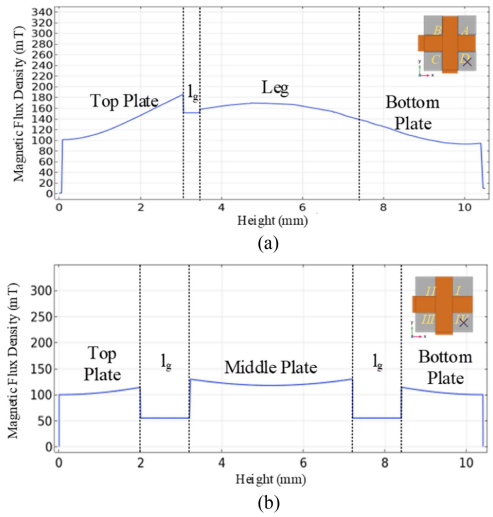

Fig. 11. Axial distribution of magnetic flux density along the z-axis, height of the structure for 5 A_{peak} current with "X" marking the point of measurement for; (a) leg D of the quadratic-legs structure, (b) quadrant IV of the legless structure.

of both the magnetic devices (see marked by "X" in Fig. 10). Fig. 11 shows an axial B-field distribution with respect to the height of the core structure for 5 A_{peak} of excitation current, with the arc length through the center of quadrant IV for the leg-less structure and leg D for the quadratic-legs structure (see marked by "X"' in Fig. 11). The legs of the quadratic-leg structure and the quadrants of the leg-less structure are also marked in three-dimensional structure view provided in Fig. 2(a) and (b), respectively.

Through the center, the maximum B-field at the top surface of the bottom plate in the quadratic-leg structure reaches 240 mT [see Fig. 10(a)], while in the leg-less structure, it reaches 200 mT on the surfaces of the middle plate [see Fig. 10(b)], which is 16.67% lower. In the quadratic-leg structure, the maximum B-field through the center of leg D is 220 mT on the bottom surface of the top plate facing the leg [see Fig. 11(a)], which is 45.45% higher than the B-field in the top plate of leg-less structure [see Fig. 11(b)]. Additionally, the magnetic flux density through quadrant IV in the middle plate of the leg-less structure [see Fig. 11(b)] is 31.6% lower than the maximum B-field in the leg of the quadratic-leg structure [see Fig. 11(a)]. Overall, the spatial average magnetic flux density in the leg-less structure is 25% lower than in the quadratic-leg structure.

For the leg-less structure to have the same intensity as the quadratic-legs structure, the excitation current through the inductive coils needs to be increased to 8 A. The spatial distribution of B-field within the three-plate, leg-less structure, for an excitation current of 8 A is shown in Fig. 12(a), and (b) is an axial distribution of B-field through the center of the magnetic structure while Fig. 12(c) is the axial distribution of B-field in quadrant IV, against the height of the structure, for the same current.

Uniformity of the B-field through the entire core and the moderate concentrations allow the magnetic device to handle more current and stronger H-field before reaching the knee (saturation point) of the B-H curve. The uniform distribution of B-field is

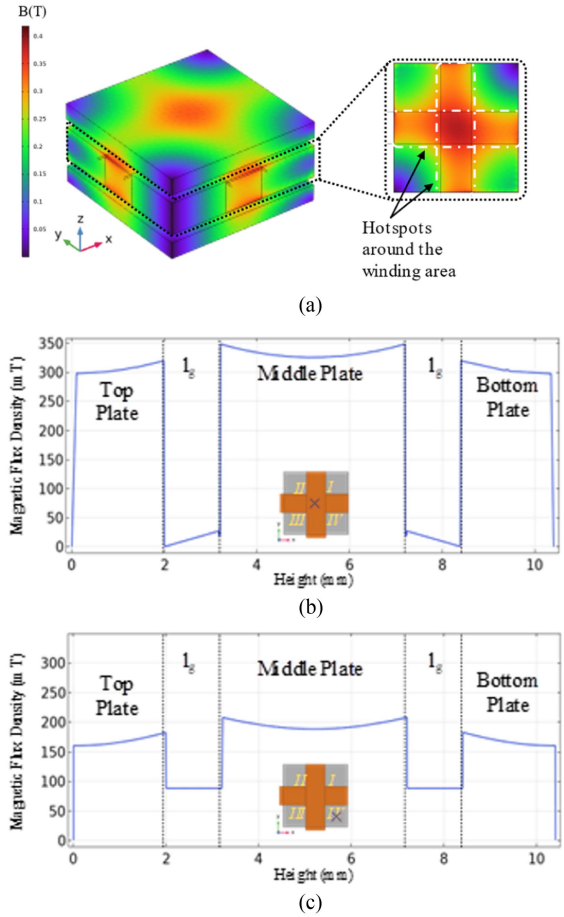

Fig. 12. B-field distribution in the leg-less structure for an excitation current of 8 A_{peak} through the inductive coils. (a) Spatial distribution of B-field. (b) Axial distribution of B-field against the height through the center of the magnetic device. (c) Axial distribution of B-field against the height through quadrant IV of the magnetic device.

crucial for maintaining the optimal magnetic permeability and reluctance of the structure, ensuring the best performance of the inductor during the operation.

For the same value of inductance and the same current passing through the inductive coils of the two structures, the power density of the two structures is the same, as both devices share the same volume. However, the leg-less structure has a higher saturation current, meaning that the device can handle higher values of current before reaching saturation point. Therefore, it can be concluded that at the maximum (saturation) current, I_{sat} for the two devices, the three-plates, leg-less structure has a higher energy and power density for the same volume of the magnetic device.

C. Flux Optimization

The choice of the three-plate, leg-less structure was motivated by its air gap flexibility and uniform distribution of magnetic flux density across the plates and higher saturation current. The legs of the quadratic-legs structure are transformed to a third plate. This transformation relieves the hot spots by ensuring an even distribution of magnetic flux throughout the structure. This leads

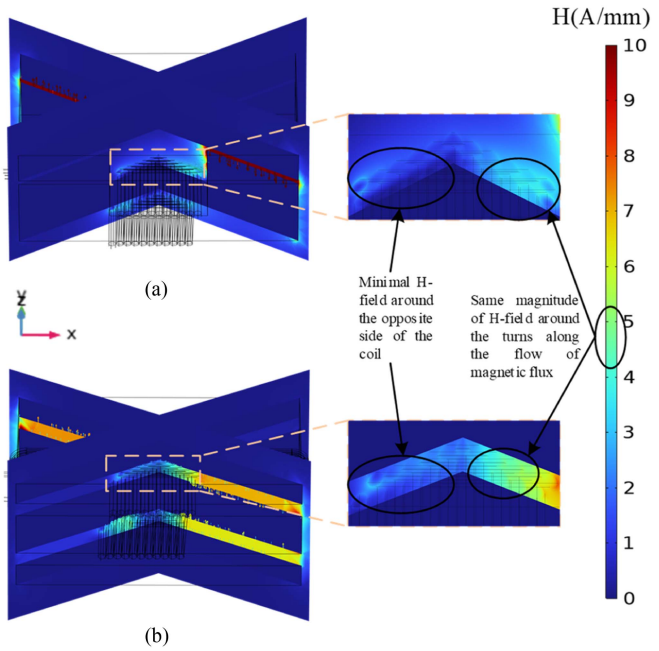

Fig. 13. Diagonal cross-sectional view of the magnetic devices illustrating the flow of H-field through the core and the concentration of H-field around the coils' turns for same excitation current of 1 A_{peak} at 35 kHz. (a) Quadratic-leg structure. (b) Leg-less structure.

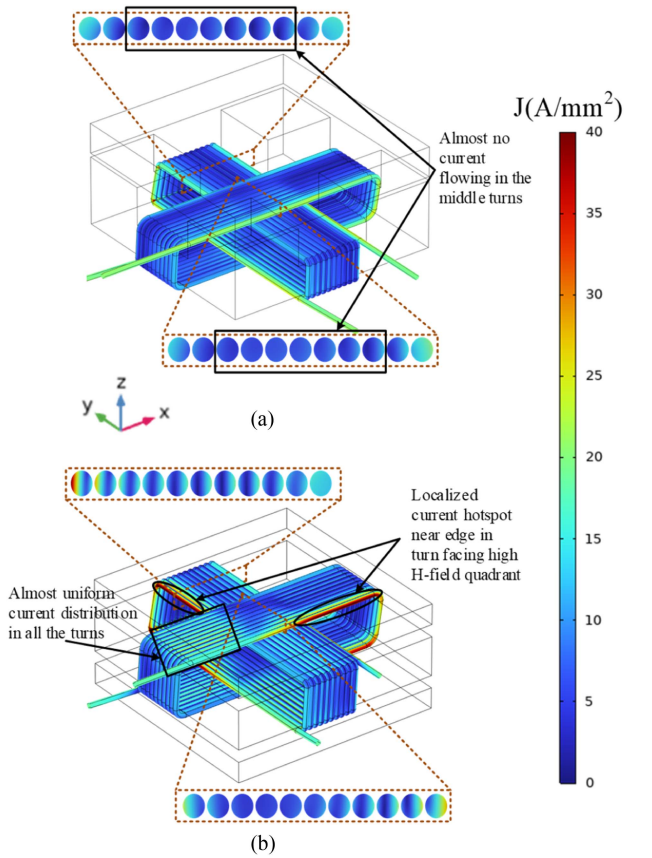

Fig. 14. Current density in the coils for an excitation current of 1 A_{peak} at 35 kHz for; (a) quadratic-leg structure showing almost no current flowing through the middle turns contributing to rise in resistance, (b) leg-less structure illustrating the localized current density hotspots around the outer edge of the structure in turns facing the quadrant with high H-field.

to the lower magnetic flux density within the core of the same volume and inductance, thereby leading to higher saturation current. Increasing the current capacity for the device by removing the legs and introducing a third plate is supposed to increase the power density of the device, as evident by FEM results.

D. Device Losses

The fringing flux reduces the magnetic reluctance of the device, thereby increasing the inductance by the fringing factor. However, it is also expected to increase the winding losses of the device because the windings are in the vicinity of the airgap with the fringing flux penetrating the winding in the transverse direction.

The magnetic and the electrical losses of the quadratic-leg structure and the leg-less structure are calculated using FEM analysis and compared with each other. The magnetic flux for both the cores flows diagonally through the magnetic core, resulting in a high H-field concentration in two quadrants of the air gap between the plates of the leg-less structure and two legs of the quadratic-leg structure while the other two quadrants and the legs experience little to no H-field, as depicted in Fig. 13. This diagonal flux path causes the coils' turns facing the high H-field quadrants (or legs) to exhibit increased current density, while the other side of the coil maintains a more uniform current distribution, as illustrated in Fig. 14. Consequently, the localized current hotspots in the high H-field regions are balanced by the low ac resistance areas on the opposite side.

In the leg-less structure, the flux lines travel straight through the air gap from plate to plate, concentrating current hotspots toward the outer edge of the device. This behavior contrasts with the quadratic-leg structure, where the H-field is more concentrated around the coil turns facing the legs, causing an increased current density throughout the length of the plate and resulting in higher ac resistance.

The electrical losses P_e in both devices are primarily determined by the winding resistance, which includes contributions from dc resistance, skin effect losses, proximity effect losses due to interactions between windings, and eddy current losses induced by the magnetic field. Given that both devices use winding cables with the same cross-sectional area and operate at the same frequency, the skin effect losses are the same. Additionally, the proximity effect losses, arising from the interaction between the two layers of coils, are also consistent due to the identical winding patterns.

Therefore, any differences in the winding resistance between the two devices are attributed to the eddy current losses induced by the time-varying magnetic field. The winding resistances for both devices are provided in Table III, which reports the average resistance of the two windings for each device.

At a switching frequency of 35 kHz and with a low number of turns (N = 3), the ac resistance of the leg-less structure's coils is approximately 20% lower than that of the quadratic-leg structure. This reduction leads to electrical losses in the leg-less

TABLE III
MAGNETIC DEVICE RESISTANCE

		Resistance (mΩ)				
Frequency(kHz)		DC	35	350	500	1000
Number of Turns (N)						
3	Quadratic-leg	11.8	326.65	1809.1	1901.8	2121.95
	Leg-less	12.3	263.3	1791.95	1919	2154.85
10	Quadratic-leg	39.3	2451.4	8403.25	9109.5	10 799
	Leg-less	41	2027.5	8023.1	8828.6	10 561

structure being correspondingly 20% lower due to its reduced resistance. However, at a frequency ten times higher (350 kHz), the electrical losses in the leg-less structure increase to nearly match those of the quadratic-leg structure, with only a 1% difference between them. For a larger number of turns (N = 10) at the same low frequency (35 kHz), the leg-less structure continues to outperform, with electrical losses still 17% lower than those of the quadratic-leg structure. At an extremely high frequency (1 MHz), the difference in electrical losses between the two structures narrows further, with the leg-less structure maintaining a slight edge of 2% lower resistance. This analysis underscores the significant efficiency benefits of the leg-less structure, particularly at lower frequencies and with fewer turns, while also highlighting its competitive performance at higher frequencies.

The magnetic losses per unit volume, $P_v(t)$ are calculated using "improved Generalized Steinmetz Equation", given in (11) to accurately capture losses associated with the triangular waveform of the boost converter [38]

$$P_v(t) = \frac{1}{T}\int_0^T k_i \left|\frac{dB}{dt}\right|^{\alpha} (\Delta B)^{\beta-\alpha} dt \tag{11}$$

where $P_v(t)$ is the time-average power loss per unit volume, dB/dt is the temporal derivative of $B(t)$, ΔB is the ripple of the magnetic flux density, T is the period of $B(t)$, and k_i is a coefficient, given by

$$k_i = \frac{k}{(2\pi)^{\alpha-1}\int_0^{2\pi} |\cos\theta|^{\alpha} 2^{\beta-\alpha} d\theta}. \tag{12}$$

For the chosen core material, TDK N97, the Steinmetz coefficients, k, α, and β at temperature of 100 °C are 0.06222, 1.70675, and 2.62171, respectively. The spatially averaged magnetic flux density (B-field) in the leg-less structure is 25% lower than in the quadratic-leg structure. This reduction is attributed to the extreme hotspots around the legs of the quadratic-leg structure, which significantly increase the spatially averaged magnetic flux density. Consequently, using (11), for the same magnetic material and operating frequency in both devices of identical volume, the magnetic losses in the leg-less structure are approximately 44% lower than those in the quadratic-leg structure.

The addition of a "shoulder" with high permeability material at the ends of the I-core [39], is intended to create a low reluctance path, thereby collecting a significant portion of the magnetic flux. However, due to the limited area of the shoulder and the low permeability outside this region, this design can lead to flux crowding. This concentration of flux in the shoulder area can result in localized hotspots and magnetic saturation, which may adversely affect the performance and efficiency of the core.

In summary, the leg-less structure demonstrates significant advantages in reducing both electrical and magnetic losses at lower frequencies and moderate turn counts. At 35 kHz, it shows 20% lower electrical losses for N = 3 and 17% lower for N = 10 compared to the quadratic-leg structure. As the frequency increases to 350 kHz and 1 MHz, the difference in electrical losses diminishes due to the skin effect, but the leg-less structure consistently maintains lower magnetic losses, approximately 44% lower, due to a 25% reduction in the spatially averaged magnetic flux density.

TABLE IV
HARDWARE PARAMETERS

Symbol	Quantity	Value
Circuit		
Vin	input voltage	0 – 70 V
D	duty cycle	0.5
Φ	phase shift	180°
f_{sw}	switching frequency	35 kHz
L_1, L_2	inductance	80 µH
C_{dc}	input capacitor	2.2 mF
C_{out}	output capacitor	50 µF
R_{load}	load	35 Ω
Inductor		
l	plate length	32 mm
w	plate width	20 mm
h	core height	16.65 mm
$t_{top,bottom}$	top/bottom plate thickness	3 mm
t_{middle}	middle plate thickness	6 mm
	core material	N97 (TDK)
μ_r	relative permeability	2300
l_g	air gap length	1.5 mm

IV. HARDWARE VALIDATION

A two-phase interleaved boost converter was chosen to test the three-plate, leg-less integrated magnetic device proposed in this article. Aims of the hardware tests are: 1) to verify the decoupling effect between the two inductive coils, 2) to investigate the hysteresis curve of the integrated magnetic device during single excitation and dual excitation of the inductive coils, and 3) to compare the circuit efficiency of the topology with the discrete core inductors. The circuit parameters are shown in Table IV. Fig. 15 shows the hardware prototype of the integrated three-plate magnetic device with the magnetic device's component parts and the discrete inductors of the same geometry.

To quantitatively determine the coupling between the two coils of the magnetic device, open and short circuit tests were conducted using COMSOL multiphysics and 4194 A Impedance Analyzer. Equation (13) [40] is used to calculate the magnetic coupling coefficient, denoted as k, between the coils. where, L_{oc} stands for the open circuit inductance, and L_{sc} stands for short circuit inductance

$$k = \sqrt{1 - \frac{L_{sc}}{L_{oc}}}. \tag{13}$$

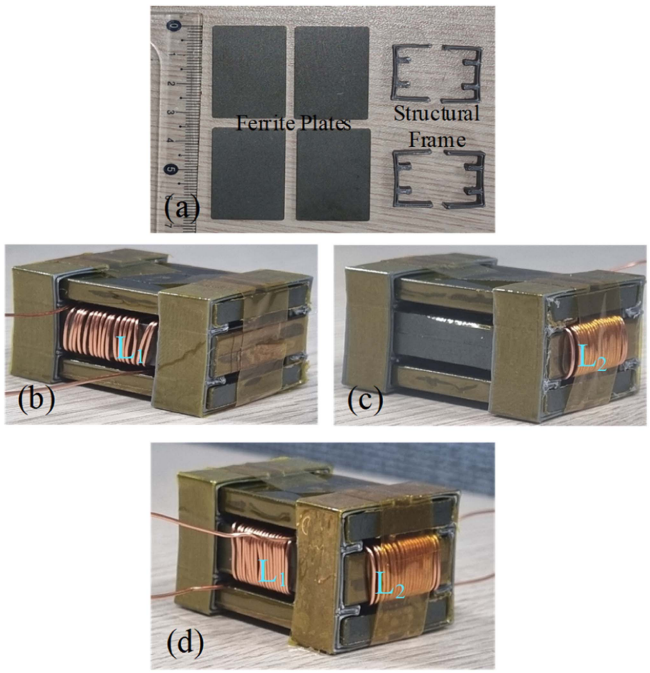

Fig. 15. (a) Components of the proposed integrated inductor, including ferrite plates and structural frame. (b) and (c) Depict conventional discrete inductors L1 and L2, respectively. (d) Proposed integrated inductor design, combining L1 and L2 within a shared integrated magnetic device.

TABLE V
MAGNETIC COUPLING TEST

	L_{oc} (μH)	L_{sc} (μH)	k
Inductor 1 (L_1)	81.43	81.429	0.0035
Inductor 2 (L_2)	81.6	81.594	0.00857

Both simulation and hardware results agree, indicating that the magnetic coupling between the coils is less than 0.01. Ideally, the coupling between the coils should be zero. However, the slight coupling in the observation is primarily attributed to electrostatic interactions rather than magnetic interactions. The measured values of open circuit and short circuit inductance are given in Table V.

An integrator circuit was used to plot the hysteresis curve of the magnetic core during single and dual excitations of the inductive coils. For the single excitation part of the experiment, only the discrete inductors [see Fig. 15(b) and (c)] were excited individually. The hysteresis loop of the excited coil was observed along with the inductor current. The objective was to get reference data for comparison and analysis with the dual excitation of the coils. Fig. 16 shows the hysteresis loop and the inductor current of inductor 1 (L_1) during the single excitation.

In the following phase of the experiment, both coils were simultaneously excited with an interleaved boost converter. It should be noticed that the individual levels of interleaved converters operate with 180° phase shift so the excitation to the inductors of the integrated magnetic device is 180° out-of-phase. Saturation currents for the coils under this dual, out-of-phase excitation were recorded. The results reveal that the saturation

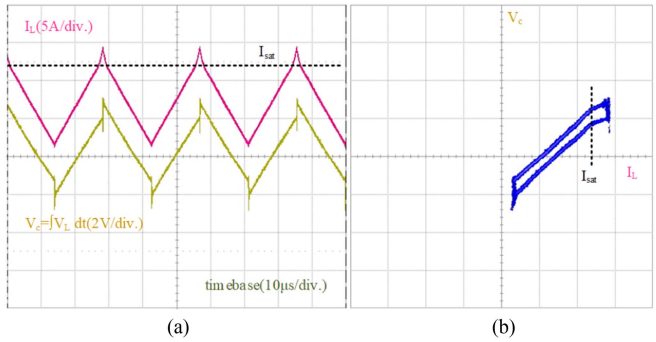

Fig. 16. Inductor 1 (see L_1 in Fig. 15(b)) waveforms during single excitation, single phase operation. (a) Current waveform. (b) B-H curve.

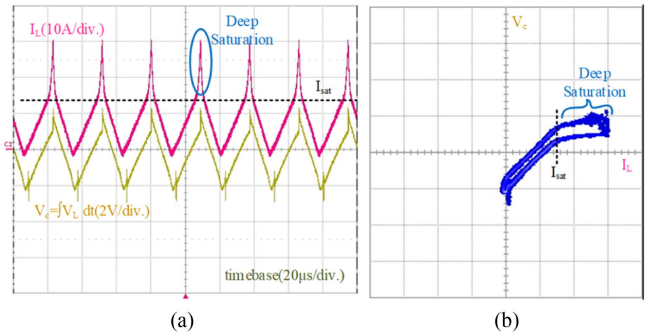

Fig. 17. Inductor 1 [see L_1 in Fig. 15(d)] waveforms during dual excitation, dual phase (interleaved) operation. (a) Current waveform. (b) B-H curve.

currents for each individual coil remains unaltered, during the interleaved converter operation. Fig. 17 shows the waveforms for inductor 1 during the saturation of the core under dual excitation.

The commercially available power inductors used for comparison are Coilcraft models AGP4233-104ME [41] and XGL1712-823MED [42]. Additionally, a comparison is made with discrete three-plate inductors using the same core geometry (see Fig. 15(b) and (c)) as the proposed device. The commercially available inductors are chosen with respect to inductance. Table VI provides a comprehensive comparison of the specifications for Coilcraft AGP4233-104ME, Coilcraft XGL1712-823MED, discrete three-plate inductors (same core geometry as the proposed device) [see Fig. 15(b) and (c)] and proposed leg-less structure magnetic device [see Fig. 15(d)].

Integrating inductors into a single magnetic core using an orthogonal winding pattern significantly reduces the overall volume of the magnetic device. This integration effectively doubles the power density, as it maintains the electrical performance of the inductors while significantly reducing the volume, offering a substantial improvement over conventional discrete inductor configurations. From Table VI, the total core volume of the proposed integrated magnetic device is 10.66 cm^3, which is significantly lower than the volume of the AGP4233-104ME (39.39 cm^3) and half the combined volume of two discrete inductors (each 10.66 cm^3, total 21.32 cm^3). This results in a substantial reduction in the overall device size, essentially doubling the energy density of the magnetic device. The saturation current

TABLE VI
MAGNETIC DEVICES COMPARISON

Device	Inductance L (uH)	Saturation Current Isat (A)	Dimensions *lxwxh* (mm)	Volume V (cm^3)	DCR (mΩ)	Energy Density (J/m^3)
AGP4233-104ME[41]	100	6.88	35.8×39.3×28	39.39	2.95	60.1
XGL1712-823MED[42]	82	5.3	18.2×17.2×12	3.76	38.4	306.3
Discrete Inductor 1	81.43	12.2	32×20×16.65	10.66	80.56	568.48
Discrete Inductor 2	81.6	12.34	32×20×16.65	10.66	130	582.82
Proposed Integrated Magnetic Device	L_1 = 81.4 L_2 = 81.6	I_{satL1} = 12.8 I_{satL2} = 12.43	32×20×16.65	10.66	L_1 = 81.3 L_2 = 131.6	1216.9

TABLE VII
VOLUME REDUCTION FOR THE PROPOSED DEVICE W/ CONVERTER OPERATING CONDITION

Converter Operating Condition	Normalized Volume		Reduction in Volume (%)
	Discrete Inductor	Integrated Inductor	
In-Phase	1+1	1.4	30
Interleaved with 0.5D	1+1	1	50
Interleaved with 0.9D	1+1	1.1	45

of each individual inductor within the integrated magnetic device (12 A) remains equivalent to that of the discrete inductors, ensuring no performance degradation in terms of handling peak currents. Additionally, the saturation current of the proposed magnetic device is almost double that of the Coilcraft inductors in Table VI.

The power density enhancement and volume reduction depend on the vector summation of the individual inductors' magnetic flux density (B-field) in the integrated magnetic device. Fig. 6 illustrates the relationship between the duty cycle during interleaved operation—where inductor currents are 180° out of phase—and the maximum effective magnetic field (B-field). The minimum maximum B-field, normalized to 1 (where only one inductor's B-field contributes to the effective B-field), is observed at a 0.5 duty cycle. At duty cycles of 0.1 and 0.9, the effective maximum B-field increases by 9.4%, as depicted in Fig. 6.

Consequently, the effective volume reduction of the integrated device is detailed in Table VII, with the volume of a single inductive device normalized to 1. Table VII shows that the maximum volume reduction reaches 50% during operation at a 0.5 duty cycle. In contrast, during in-phase operation, the effective volume reduction is 30%. For duty cycles of 0.1 and 0.9, the volume reduction achieves 45%.

The practical tests conducted using the experimental circuit demonstrate that the two orthogonal inductors within the proposed integrated magnetic device operate independently of each other during 180° out-of-phase (interleaved) operation with any duty cycle. This independence ensures that the saturation currents for each inductor remain consistent with those of the discrete inductors.

The proposed leg-less structure not only reduces the physical footprint and volume of the magnetic device but also enhances the power density by 100% because the integrated magnetic device effectively reduces the volume of the magnetic components in the converter by half, without compromising the electrical performance in terms of inductance, saturation current, and dc resistance.

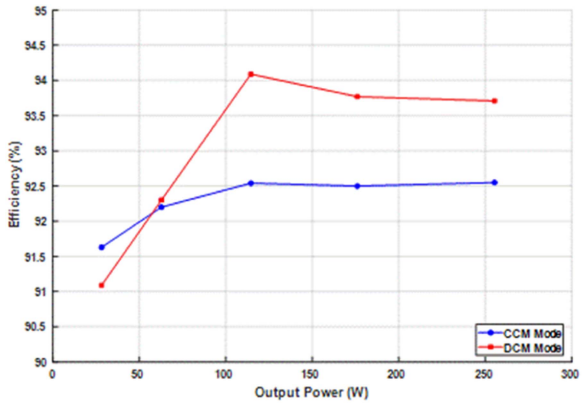

Fig. 18. Efficiency curve of the converter for different operating modes.

To assess the feasibility of the integrated magnetic device, an efficiency test was conducted on the designed interleaved boost converter topology with input voltage, V_{in} of 30 V. Two distinct inductors, sharing identical inductance values with the respective inductors of the integrated inductor and constructed from the same core material [see Fig. 15(b) and (c)], were incorporated into the interleaved boost converter design. The circuit's efficiency was measured at different output power and the efficiency curves for both CCM and DCM operation are shown in Fig. 18. The tests revealed that the circuit operated with an efficiency of 94% with both the integrated and discrete inductors.

V. CONCLUSION

In this article, an improved, three-plates, cubic, leg-less integrated magnetic device is proposed featuring two coils wound orthogonally in space, on a single magnetic core. Despite sharing the same magnetic core, the unique alignment of the coils ensures the absence of magnetic coupling between them, effectively transforming the coils into two independent inductors. FEM results are provided to comprehend the behavior of magnetic flux density inside the core volume. The proposed three-plates, leg-less structure outperforms the two-plates, quadratic-legs structure, both in terms of electrical and magnetic losses. Open circuit and short circuit tests are performed to quantitatively determine the level of coupling between the coils. The tests reveal that the magnetic coupling between the coils is remarkably low, measuring less than 0.01. Hardware experimentation is performed to investigate the saturation of the integrated inductive device using interleaved boost converter. The interleaved operation of the topology and DCM mode ensures that the

hysteresis loops for the two perpendicular inductive coils remain unaffected during the dual phase operation of the converter. Efficiency of the topology with the proposed integrated device is compared with the topology utilizing discrete inductors. The results of the efficiency test include a promising potential of the proposed inductive device. The results affirm the capability of the proposed integrated magnetic device as a replacement for interleaved topologies, reducing the volume of the magnetic component by half with no compromise to the efficiency of the system. Thereby, greatly reducing the overall size, weight and cost of the system. This not only highlights the robustness of the design but also places it as an efficient and space-saving solution for various applications. The idea opens avenues for further exploration and optimization of magnetic devices with dual-coil configurations, emphasizing the importance of phase separation and structural considerations in achieving optimal system performances.

REFERENCES

[1] M. A. Tawfik, M. Ehab, A. Ahmed, and J.-H. Park, "Single-stage isolated DC/AC converter with continuous dynamic model and controller design," *IEEE Trans. Ind. Electron.*, vol. 70, no. 6, pp. 5971–5981, Jun. 2023, doi: 10.1109/TIE.2022.3196375.

[2] J. D. van Wyk and F. C. Lee, "On a future for power electronics," *IEEE J. Emerg. Sel. Topics Power Electron.*, vol. 1, no. 2, pp. 59–72, Jun. 2013.

[3] M. Ehab, M. A. Tawfik, M. U. Munir, A. Ahmed, and J.-H. Park, "ISM-band frequency transformer modeling for isolated high-power conversions," *IEEE Trans. Instrum. Meas.*, vol. 72, Mar. 2023, Art. no. 8002111, doi: 10.1109/TIM.2023.3261921.

[4] M. Khodabandeh, E. Afshari, and M. Amirabadi, "A Family of Ćuk, Zeta, and SEPIC based soft-switching DC–DC converters," *IEEE Trans. Power Electron.*, vol. 34, no. 10, pp. 9503–9519, Oct. 2019, doi: 10.1109/TPEL.2019.2891563.

[5] M. Forouzesh, Y. P. Siwakoti, S. A. Gorji, F. Blaabjerg, and B. Lehman, "Step-up DC–DC converters: A comprehensive review of voltage-boosting techniques, topologies, and applications," *IEEE Trans. Power Electron.*, vol. 32, no. 12, pp. 9143–9178, Dec. 2017, doi: 10.1109/TPEL.2017.2652318.

[6] R. R. Khorasani et al., "An interleaved soft switched high step-up boost converter with high power density for renewable energy applications," *IEEE Trans. Power Electron.*, vol. 37, no. 11, pp. 13782–13798, Nov. 2022, doi: 10.1109/TPEL.2022.3181946.

[7] J. Imaoka et al., "A magnetic design method considering DC-biased magnetization for integrated magnetic components used in multiphase boost converters," *IEEE Trans. Power Electron.*, vol. 33, no. 4, pp. 3346–3362, Apr. 2018, doi: 10.1109/TPEL.2017.2707385.

[8] M. U. Munir et al., "Loss analysis of nanocrystalline cores for high frequency transformer in power electronics circuits," *J. Electr. Eng. Technol.*, vol. 19, pp. 1257–1266, 2023, doi: 10.1007/s42835-023-01711-9.

[9] C. Jiang, X. Li, S. S. Ghosh, H. Zhao, Y. Shen, and T. Long, "Nanocrystalline powder cores for high-power high-frequency power electronics applications," *IEEE Trans. Power Electron.*, vol. 35, no. 10, pp. 10821–10830, Oct. 2020, doi: 10.1109/TPEL.2020.2979069.

[10] M. Ehab, M. A. Tawfik, C.-G. Lee, A. Ahmed, and J.-H. Park, "Performance of the 100-μm diameter high conductivity CNT fibers in MHz frequencies," *IEEE Trans. Nanotechnol.*, vol. 21, pp. 466–473, Aug. 2022, doi: 10.1109/TNANO.2022.3200640.

[11] J. H. Park et al., "Performance evaluation of carbon nanotube yarn-based inductors for ISM-frequency band soft-switching converters," *J. Power Electron.*, vol. 23, pp. 1778–1788, 2023, doi: 10.1007/s43236-023-00693-1.

[12] H. Chen, B. Wei, and D. Ma, "Energy storage and management system with carbon nanotube supercapacitor and multidirectional power delivery capability for autonomous wireless sensor nodes," *IEEE Trans. Power Electron.*, vol. 25, no. 12, pp. 2897–2909, Dec. 2010, doi: 10.1109/TPEL.2010.2081380.

[13] G. Calderon-Lopez, A. J. Forsyth, and D. R. Nuttall, "Design and performance evaluation of a 10-kW interleaved boost converter for a fuel cell electric vehicle," in *Proc. CES/IEEE 5th Int. Power Electron. Motion Control Conf.*, Shanghai, China, 2006, pp. 1–5, doi: 10.1109/IPEMC.2006.4778205.

[14] K. J. Hartnett, M. S. Rylko, J. G. Hayes, and M. G. Egan, "A comparison of classical two phase (2L) and transformer — Coupled (XL) interleaved boost converters for fuel cell applications," in *Proc. 25th Annu. IEEE Appl. Power Electron. Conf. Expo.*, Palm Springs, CA, USA, 2010, pp. 787–793, doi: 10.1109/APEC.2010.5433580.

[15] M. Hirakawa, M. Nagano, Y. Watanabe, K. Andoh, S. Nakatomi, and S. Hashino, "High power density DC/DC converter using the close-coupled inductors," in *Proc. IEEE Energy Convers. Congr. Expo.*, San Jose, CA, USA, 2009, pp. 1760–1767, doi: 10.1109/ECCE.2009.5316389.

[16] Y. Li and S. Sathiakumar, "Quadratic DC-DC boost converter using coupled inductors for high step-up ratio," in *Proc. Asia Model. Symp.*, pp. 133–138, 2017.

[17] P.-W. Lee, Y.-S. Lee, D. K. W. Cheng, and X.-C. Liu, "Steady-state analysis of an interleaved boost converter with coupled inductors," *IEEE Trans. Ind. Electron.*, vol. 47, no. 4, pp. 787–795, Aug. 2000, doi: 10.1109/41.857959.

[18] T.-F. Wu, Y.-S. Lai, J.-C. Hung, and Y.-M. Chen, "Boost converter with coupled inductors and buck–Boost type of active clamp," *IEEE Trans. Ind. Electron.*, vol. 55, no. 1, pp. 154–162, Jan. 2008.

[19] Y. Zhao, W. Li, B. Yang, and X. He, "Active clamp boost converter with switched capacitor and coupled inductor," in *Proc. 25th Annu. IEEE Appl. Power Electron. Conf. Expo.*, 2010, pp. 801–806.

[20] H. Liu, H. Hu, H. Wu, Y. Xing, and I. Batarseh, "Overview of high-step-up coupled-inductor boost converters," *IEEE J. Emerg. Sel. Topics Power Electron.*, vol. 4, no. 2, pp. 689–704, Jun. 2016.

[21] X. Huang et al., "Parasitic ringing and design issues of high power interleaved boost converters," in *Proc. IEEE 33rd Annu. IEEE Power Electron. Specialists Conf.*, 2002, vol. 1, pp. 30–35.

[22] W. Li and X. He, "An interleaved winding-coupled boost converter with passive lossless clamp circuits," *IEEE Trans. Power Electron.*, vol. 22, no. 4, pp. 1499–1507, Jul. 2007.

[23] S. Dwari and L. Parsa, "An efficient high-step-up interleaved DC–DC converter with a common active clamp," *IEEE Trans. Power Electron.*, vol. 26, no. 1, pp. 66–78, Jan. 2011.

[24] P. Saadat and K. Abbaszadeh, "A single-switch high step-up DC–DC converter based on quadratic boost," *IEEE Trans. Ind. Electron.*, vol. 63, no. 12, pp. 7733–7742, Dec. 2016, doi: 10.1109/TIE.2016.2590991.

[25] K. J. Hartnett, J. G. Hayes, M. G. Egan, and M. S. Rylko, "CCTT-core split-winding integrated magnetic for high-power DC–DC converters," *IEEE Trans. Power Electron.*, vol. 28, no. 11, pp. 4970–4984, Nov. 2013, doi: 10.1109/TPEL.2013.2240394.

[26] Y. Liu et al., "Optimized air-gap configuration for an integrated coupled inductor with lower height and reduced core/winding losses," *IEEE Trans. Ind. Appl.*, vol. 60, no. 2, pp. 2980–2990, Mar./Apr. 2024.

[27] P. Zumel, O. Garcia, J. A. Cobos, and J. Uceda, "Magnetic integration for interleaved converters," in *Proc. 18th Annu. IEEE Appl. Power Electron. Conf. Expo.*, Miami Beach, FL, USA, 2003, vol. 2, pp. 1143–1149, doi: 10.1109/APEC.2003.1179360.

[28] W. Huang and B. Lehman, "Inversely coupled inductors with small volume and reduced power loss for switching converters," *IEEE Trans. Power Electron.*, vol. 38, no. 6, pp. 6779–6783, Jun. 2023, doi: 10.1109/TPEL.2023.3241883.

[29] B. N. Sanusi and Z. Ouyang, "Integrated inductor design for a highly compact embedded battery charger," *IEEE Trans. Power Electron.*, vol. 37, no. 8, pp. 8873–8885, Aug. 2022, doi: 10.1109/TPEL.2022.3156372.

[30] Z. Ouyang, Z. Zhang, M. A. E. Andersen, and O. C. Thomsen, "Four quadrants integrated transformers for dual-input isolated DC–DC converters," *IEEE Trans. Power Electron.*, vol. 27, no. 6, pp. 2697–2702, Jun. 2012.

[31] Y. Dou, Z. Ouyang, and M. A. E. Andersen, "Integrated coupled inductors with functionality of current balancing transformer for two-phase synchronous DC-DC converters," *IEEE Trans. Power Electron.*, vol. 35, no. 5, pp. 4472–4476, May 2020.

[32] Z. Ouyang, O. C. Thomsen, M. A. E. Andersen, and T. Björklund, "New geometry integrated inductors in two-channel interleaved bidirectional converter," in *Proc. IEEE 36th Annu. Conf. IEEE Ind. Electron.*, Phoenix, AZ, USA, 2010, pp. 582–586.

[33] S. Petersen, "Improved geometry of integrated magnetics for the hybridge topology," in *Proc. ESA*, 2002, pp. 241–246.

[34] P. Kinsler, "Faraday's law and magnetic induction: Cause and effect, experiment and theory," *Physics*, vol. 2, no. 2, pp. 150–163, 2020.

[35] M. K. Kazimierczuk, "Effect of fringing flux on inductance for rectangular air gap," in *High Frequency Magnetic Components*, 2nd ed. Hoboken, NJ, USA: Wiley, 2014, pp. 58–59.
[36] M. K. Kazimierczuk, "Air gap in magnetic core," in *High Frequency Magnetic Components*, 2nd ed. Hoboken, NJ, USA: Wiley, 2014, pp. 51–54.
[37] M. K. Kazimierczuk, "Core saturation," in *High Frequency Magnetic Components*, 2nd ed. Hoboken, NJ, USA: Wiley, 2014, pp. 32–34.
[38] L. Havez, E. Sarraute, and Y. Lefevre, "3D Power inductor: Calculation of iron core loss," in *Proc. COMSOL Conf.*, 2013. [Online]. Available: https://www.comsol.com/paper/3d-power-inductor-calculation-of-iron-core-losses-15484
[39] Z. Ouyang, O. C. Thomsen, M. A. E. Andersen, and T. Björklund, "Low profile, low cost, new geometry integrated inductors," in *Proc. IEEE Appl. Power Electron. Conf. Expo.*, Fort Worth, U.S.A, 2011, pp. 150–156.
[40] C. Degen, "Inductive coupling for wireless power transfer and near-field communication," *J. Wireless Commun. Netw.*, vol. 2021, 2021, Art. no. 121, doi: 10.1186/s13638-021-01994-4.
[41] TH Power Inductors – AGP4233, Coilcraft, 2022. [Online]. Available: https://www.coilcraft.com/en-us/products/power/shielded-inductors/high-current-flat-wire/agp-ver/agp4233
[42] Shielded Power Inductors – XGL1712, Coilcraft, 2023. [Online]. Available: https://www.coilcraft.com/en-us/products/power/shielded-inductors/molded-inductor/xgl/xgl1712/

Shamroze Fayyaz received the B.Sc. degree in electrical and electronics engineering from European University of Lefke, Ankara, Türkiye, in 2020. He is currently working toward the the M.Sc. degree in power electronics with the Department of Electrical Engineering, Soongsil University, Seoul, South Korea.

His research interests include the analysis, design, and development of high frequency switching power converters and integrated magnetics.

Umair Munir received the B.Sc. degree in electrical and electronics engineering from European University of Lefke, Ankara, Türkiye, in 2020, and the M.Sc. degree in electrical engineering from Soongsil University, Seoul, South Korea, in 2024.

His research interests include the analysis, design, and development of high frequency switching power converters, high voltage plasma circuits, and integrated approaches for power converters.

Mr. Munir was a recipient of the prestigious Global Korea Scholarship Award for graduate studies.

Mohamed Atef Tawfik received the B.S. degree in electrical engineering from the Department of Electrical Engineering, Assiut University, Asyut, Egypt, in 2013, and the M.S. degree in electrical engineering from Soongsil University, Seoul, South Korea, in 2020. He is currently working toward the Ph.D. degree in electrical engineering with Soongsil University, Seoul, South Korea.

He was a Research Assistant with the Renewable Energy Department, Desert Research Center, Cairo, Egypt, during 2014–2018. His current research interests include the analysis and design of switching power converters for renewable energy applications.

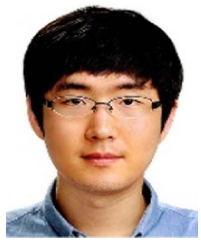

Kyoung-Tak Kim was born in Seoul, South Korea, in 1988. He received the B.S. and M.S. degrees in electrical engineering in 2016 from Soongsil University, Seoul, South Korea, where he is currently working toward the Ph.D. degree in electrical engineering.

His research interests include the development of carbon nanotube material for power electronics, cyber-physical security for solar inverter with power system, deep learning algorithm for arc fault detection device.

Jong-Kwon Jeon received the B.S. degree in electrical engineering from Hoseo University, Cheonan, South Korea, in 2024. He is currently working toward the master's degree in electrical engineering from Soongsil University, Seoul, South Korea.

His current research interests include the analysis and design of single stage power converter topologies and control strategies.

Ashraf Ahmed (Member, IEEE) received the B.Sc. degree from Assiut University, Asyut, Egypt, in 1999, and the M.Sc. degree from Cairo University, Giza, Egypt, in 2005, both in electrical engineering, and the Ph.D. degree in electrical engineering from the University of Durham, Durham, U.K., in 2011.

He is currently an Assistant Professor with Soongsil University, Seoul, South Korea. His research interests include the analysis and design of switching power converters for renewable energy applications.

Joung-Hu Park (Senior Member, IEEE) received the B.S., M.S., and Ph.D. degrees in electrical engineering from the Department of Electrical Engineering and Computer Science, Seoul National University, Seoul, South Korea, in 1999, 2001, and 2006, respectively.

He is currently an Associate Professor with Soongsil University, Seoul, South Korea. From 2004 to 2005, he was a visiting scholar with Virginia Tech, Blacksburg, VA, USA, and from 2015 to 2016, he was a visiting Assistant Professor with the University of British Columbia, Vancouver, Canada. His current research interests include the analysis of high frequency switching converters and renewable energy applications.